Research Article | Vol. 26, No. 14 | 9 Jul 2018 | OPTICS EXPRESS 18115
Optics EXPRESS

Compressed sensing FTIR nano-spectroscopy and nano-imaging

Bernd Kästner,[1,*] Franko Schmähling,[1] Andrea Hornemann,[1] Georg Ulrich,[1] Arne Hoehl,[1] Mattias Kruskopf,[1] Klaus Pierz,[1] Markus B. Raschke,[2] Gerd Wübbeler,[1] and Clemens Elster[1]

[1]*Physikalisch-Technische Bundesanstalt, Braunschweig and Berlin, Germany*
[2]*Department of Physics, Department of Chemistry, and JILA, University of Colorado, Boulder, 80309, USA*
**bernd.kaestner@ptb.de*

Abstract: Infrared scattering scanning near-field optical microscopy (IR *s*-SNOM) provides for spectroscopic imaging with nanometer spatial resolution, yet full spatio-spectral imaging is constrained by long measurement times. Here, we demonstrate the application of compressed sensing algorithms to achieve hyperspectral FTIR-based nano-imaging at an order of magnitude faster imaging speed to achieve the same spectral content compared to conventional approaches. At the example of the spectroscopy of a single vibrational resonance, we discuss the relationship of prior knowledge of sparseness of the employed Fourier base functions and sub-sampling. Compressed sensing nano-FTIR spectroscopy promises both rapid and sensitive chemical nano-imaging which is highly relevant in academic and industrial settings for fundamental and applied nano- and bio-materials research.

OCIS codes: (120.0120) Instrumentation, measurement, and metrology; (180.4243) Near-field microscopy.

References and links

1. H. Günzler and H.-U. Gremlich, *IR Spectroscopy* (Wiley-VCH, 2002).
2. R. Salzer and H. W. Siesler, eds., *Infrared and Raman Spectroscopic Imaging* (Wiley-VCH, 2014).
3. G. Downey, "Food and food ingredient authentication by mid-infrared spectroscopy and chemometrics," TrAC Trends Analyt. Chem. **17**(7), 418–424 (1998).
4. G. F. Mohsin, F.-J. Schmitt, C. Kanzler, J. Dirk Epping, S. Flemig, and A. Hornemann, "Structural characterization of melanoidin formed from d-glucose and l-alanine at different temperatures applying FTIR, NMR, EPR, and MALDI-ToF-MS," Food Chem. **245**, 761–767 (2018).
5. D. Helm, H. Labischinski, G. Schallehn, and D. Naumann, "Classification and identification of bacteria by Fourier-transform infrared spectroscopy," J. Gen. Microbiol. **137**(1), 69–79 (1991).
6. A. Hornemann, D. Sinning, S. Cortes, L. Campino, P. Emmer, K. Kuhls, G. Ulm, M. Frohme, and B. Beckhoff, "A pilot study on fingerprinting Leishmania species from the Old World using Fourier transform infrared spectroscopy," Anal. Bioanal. Chem. **409**(29), 6907–6923 (2017).
7. D. C. Fernandez, R. Bhargava, S. M. Hewitt, and I. W. Levin, "Infrared spectroscopic imaging for histopathologic recognition," Nat. Biotechnol. **23**(4), 469–474 (2005).
8. M. Born and E. Wolf, *Principles of Optics: Electromagnetic Theory of Propagation, Interference and Diffraction of Light*, 7th ed. (Cambridge University, 2002).
9. B. Knoll and F. Keilmann, "Infrared conductivity mapping for nanoelectronics," Appl. Phys. Lett. **77**(24), 3980–3982 (2000).
10. F. Keilmann and R. Hillenbrand, "Near-field nanoscopy by elastic light scattering from a tip," in *Nano-Optics and Near-Field Optical Microscopy*, A. Zayats and D. Richard, eds. (Artech House, 2009), pp. 235–265.
11. A. Hartschuh, "Tip-enhanced near-field optical microscopy," Angew. Chem. Int. Ed. Engl. **47**(43), 8178–8191 (2008).
12. F. Huth, A. Govyadinov, S. Amarie, W. Nuansing, F. Keilmann, and R. Hillenbrand, "Nano-FTIR absorption spectroscopy of molecular fingerprints at 20 nm spatial resolution," Nano Lett. **12**(8), 3973–3978 (2012).
13. A. C. Jones and M. B. Raschke, "Thermal Infrared Near-Field Spectroscopy," Nano Lett. **12**(3), 1475–1481 (2012).
14. P. Hermann, A. Hoehl, P. Patoka, F. Huth, E. Rühl, and G. Ulm, "Near-field imaging and nano-Fourier-transform infrared spectroscopy using broadband synchrotron radiation," Opt. Express **21**(3), 2913–2919 (2013).
15. H. A. Bechtel, E. A. Muller, R. L. Olmon, M. C. Martin, and M. B. Raschke, "Ultrabroadband infrared nanospectroscopic imaging," Proc. Natl. Acad. Sci. U.S.A. **111**(20), 7191–7196 (2014).

#328153 https://doi.org/10.1364/OE.26.018115
Journal © 2018 Received 13 Apr 2018; revised 24 May 2018; accepted 10 Jun 2018; published 28 Jun 2018

16. B. T. O'Callahan, W. E. Lewis, S. Möbius, J. C. Stanley, E. A. Muller, and M. B. Raschke, "Broadband infrared vibrational nano-spectroscopy using thermal blackbody radiation," Opt. Express **23**(25), 32063–32074 (2015).
17. B. Pollard, F. C. B. Maia, M. B. Raschke, and R. O. Freitas, "Infrared Vibrational Nanospectroscopy by Self-Referenced Interferometry," Nano Lett. **16**(1), 55–61 (2016).
18. I. Amenabar, S. Poly, M. Goikoetxea, W. Nuansing, P. Lasch, and R. Hillenbrand, "Hyperspectral infrared nanoimaging of organic samples based on Fourier transform infrared nanospectroscopy," Nat. Commun. **8**, 14402 (2017).
19. R. O. Freitas, C. Deneke, F. C. B. Maia, H. G. Medeiros, T. Moreno, P. Dumas, Y. Petroff, and H. Westfahl, "Low-aberration beamline optics for synchrotron infrared nanospectroscopy," Opt. Express **26**(9), 11238–11249 (2018).
20. L. Ran, Y. Zhang, W. Wei, and Q. Zhang, "A hyperspectral image classification framework with spatial pixel pair features," Sensors (Basel) **17**(10), 2421 (2017).
21. D. L. Donoho, "Compressed sensing," IEEE Trans. Inf. Theory **51**(4), 1289–1306 (2006).
22. E. J. Candés and T. Tao, "Decoding by linear programming," IEEE Trans. Inf. Theory **51**(12), 4203–4215 (2005).
23. E. J. Candés, J. Romberg, and T. Tao, "Stable signal recovery from incomplete and inaccurate measurements," Commun. Pure Appl. Math. **59**(8), 1207–1223 (2006).
24. E. J. Candés and T. Tao, "Near-optimal signal recovery from random projections: universal encoding strategies?" IEEE Trans. Inf. Theory **52**(12), 5406–5425 (2006).
25. E. J. Candés, J. Romberg, and T. Tao, "Robust uncertainty principles: exact signal reconstruction from highly incomplete frequency information," IEEE Trans. Inf. Theory **52**(2), 489–509 (2006).
26. E. J. Candés and T. Tao, "The Dantzig selector: statistical estimation when p is much larger than n," Ann. Stat. **35**(6), 2313–2351 (2007).
27. Y. C. Eldar and G. Kutyniok, eds., *Compressed Sensing: Theory and Applications* (Cambridge University Press, 2012).
28. X. Lin, G. Wetzstein, Y. Liu, and Q. Dai, "Dual-coded compressive hyperspectral imaging," Opt. Lett. **39**(7), 2044–2047 (2014).
29. X. Sui, Q. Chen, G. Gu, and X. Shen, "Infrared super-resolution imaging based on compressed sensing," Infrared Phys. Technol. **63**, 119–124 (2014).
30. Y. Mao, Y. Wang, J. Zhou, and H. Jia, "An infrared image super-resolution reconstruction method based on compressive sensing," Infrared Phys. Technol. **76**, 735–739 (2016).
31. Z. Zhang, X. Ma, and J. Zhong, "Single-pixel imaging by means of Fourier spectrum acquisition," Nat. Commun. **6**(1), 6225 (2015).
32. Y. August, C. Vachman, Y. Rivenson, and A. Stern, "Compressive hyperspectral imaging by random separable projections in both the spatial and the spectral domains," Appl. Opt. **52**(10), D46–D54 (2013).
33. I. August, Y. Oiknine, M. AbuLeil, I. Abdulhalim, and A. Stern, "Miniature compressive ultra-spectral imaging system utilizing a single liquid crystal phase retarder," Sci. Rep. **6**(1), 23524 (2016).
34. J. N. Sanders, S. K. Saikin, S. Mostame, X. Andrade, J. R. Widom, A. H. Marcus, and A. Aspuru-Guzik, "Compressed sensing for multidimensional spectroscopy experiments," J. Phys. Chem. Lett. **3**(18), 2697–2702 (2012).
35. J. J. Humston, I. Bhattacharya, M. Jacob, and C. M. Cheatum, "Compressively sampled two-dimensional infrared spectroscopy that preserves line shape information," J. Phys. Chem. A **121**(16), 3088–3093 (2017).
36. D. J. Holland, M. J. Bostock, L. F. Gladden, and D. Nietlispach, "Fast multidimensional NMR spectroscopy using compressed sensing," Angew. Chem. Int. Ed. Engl. **50**(29), 6548–6551 (2011).
37. A. S. Stern and J. C. Hoch, "A new approach to compressed sensing for NMR," Magn. Reson. Chem. **53**(11), 908–912 (2015).
38. "NMR Software by Bruker Corp.," https://www.bruker.com/products/mr/nmr/nmr-software/nmr-software.html.
39. O. Katz, J. M. Levitt, and Y. Silberberg, "Compressive Fourier transform spectroscopy," in *Frontiers in Optics 2010/Laser Science XXVI*, OSA Technical Digest (CD) (Optical Society of America, 2010), p. FTuE3.
40. A. Gottwald, R. Klein, R. Müller, M. Richter, F. Scholze, R. Thornagel, and G. Ulm, "Current capabilities at the Metrology Light Source," Metrologia **49**(2), S146–S151 (2012).
41. R. Hillenbrand and F. Keilmann, "Complex optical constants on a subwavelength scale," Phys. Rev. Lett. **85**(14), 3029–3032 (2000).
42. M. Kruskopf, D. M. Pakdehi, K. Pierz, S. Wundrack, R. Stosch, T. Dziomba, M. Götz, J. Baringhaus, J. Aprojanz, C. Tegenkamp, J. Lidzba, T. Seyller, F. Hohls, F. J. Ahlers, and H. W. Schumacher, "Comeback of epitaxial graphene for electronics: large-area growth of bilayer-free graphene on SiC," 2D Mater. **3**(4), 41002 (2016).
43. M. Kruskopf, K. Pierz, S. Wundrack, R. Stosch, T. Dziomba, C.-C. Kalmbach, A. Müller, J. Baringhaus, C. Tegenkamp, F. J. Ahlers, and H. W. Schumacher, "Epitaxial graphene on SiC: modification of structural and electron transport properties by substrate pretreatment," J. Phys. Condens. Matter **27**(18), 185303 (2015).
44. A. J. Huber, A. Ziegler, T. Köck, and R. Hillenbrand, "Infrared nanoscopy of strained semiconductors," Nat. Nanotechnol. **4**(3), 153–157 (2009).
45. P. R. Griffiths and J. A. de Haseth, *Fourier Transform Infrared Spectrometry* (Wiley, 2007).
46. S. Chen, D. Donoho, and M. Saunders, "Atomic decomposition by basis pursuit," SIAM J. Sci. Comput. **20**(1), 33–61 (1998).

47. A. Cohen, W. Dahmen, and R. DeVore, "Compressed sensing and best k-terms approximation," J. Am. Math. Soc. **22**(1), 211–231 (2009).
48. S. G. Mallat and Z. Zhang, "Matching pursuits with time-frequency dictionaries," IEEE Trans. Signal Process. **41**(12), 3397–3415 (1993).
49. H. Rue and L. Held, *Gaussian Markov Random Fields: Theory and Applications* (CRC, 2005).
50. P. Hansen and D. O'Leary, "The Use of the L-Curve in the Regularization of Discrete Ill-Posed Problems," SIAM J. Sci. Comput. **14**(6), 1487–1503 (1993).
51. S. Mastel, A. A. Govyadinov, T. V. A. G. de Oliveira, I. Amenabar, and R. Hillenbrand, "Nanoscale-resolved chemical identification of thin organic films using infrared near-field spectroscopy and standard Fourier transform infrared references," Appl. Phys. Lett. **106**(2), 23113 (2015).

1. Introduction

Optical spectroscopy, such as Fourier Transform Infrared (FTIR) spectroscopy, provides chemical material contrast based on molecular vibrations, lattice phonons, or charge carrier concentrations [1]. In particular, infrared (IR) photons in the energy range between 400 cm^{-1} and 4000 cm^{-1} (corresponding to wavelengths from 2.5 to 25 μm) allow the investigation of fundamental vibrations and the associated rotational-vibrational structure. Since chemical bonds have unique spectral signatures, 2D chemical mapping of the dense spectral content allows to identify and localize unknown constituents [2], as desired in different fields of chemistry [3,4], biology [5,6], and medicine [7]. The achievable spatial resolution of conventional IR microscopy is, however, limited to several micrometers owing to diffraction [8]. This limitation can be overcome by applying near-field based techniques, such as scattering-type scanning near-field optical microscopy (*s*-SNOM) [9–11]. *s*-SNOM is based on the principle of an atomic force microscope (AFM) and utilizes a sharp metallic tip brought into close proximity to the sample surface. By simultaneously illuminating this near-field probe with a focused light beam, the tip acts as an optical antenna which strongly confines the incident optical field around the tip apex, thus providing a nanoscale light source for high-resolution imaging and spectroscopy. A full IR spectrum at each image pixel is usually obtained by combining *s*-SNOM with FTIR spectroscopy, when using a broadband IR source in the form of laser, thermal, or synchrotron radiation (nano-FTIR) [12–19].

The acquisition of the complete spectrum has the advantage that no prior knowledge of the sample is needed since post-processing allows all available information from the data set to be mined afterward. Hyperspectral imaging can also exploit the spatial relationships among the different adjacent spectra, allowing more elaborate spectral-spatial models for a more accurate segmentation and classification of the image [20].

However, recording hyperspectral data sets is challenged by the often limited spectral irradiance of the available IR source and the long measurement time required to achieve adequate s/n ratio at each image pixel for the desired spatio-chemical sensitivity. Conventional oversampling as in FTIR microscopy, leads to prohibitively long acquisition times in nano-FTIR imaging as a necessarily sequential data acquisition process, especially when nanometer spatial resolution is desired over an appreciable field of view. The s/n ratio is further constrained by the still limited availability of intense broadband IR sources suitable for nano-FTIR *s*-SNOM, on top of the in general weak near-field signal intensities to be detected. It is therefore desirable to apply algorithms to the acquisition process to minimize data redundancy and acquire just the minimum amount of data necessary to derive a desired spectral content.

Compressed sensing (CS) [21–27] is a recent approach that can enable hyperspectral data acquisition in realistic measurement times, since it allows the complete reconstruction of a function from a reduced number of measurements provided that the unknown function has a sparse representation in a suitably chosen basis or dictionary. CS has already been successfully applied in different fields of physics, chemistry, or engineering [27]. For instance, the high potential of CS was predicted for computational imaging [28–33], FTIR spectroscopy [39], and in multidimensional nonlinear IR [34,35] and NMR spectroscopy [36,37], where the technique is already established and in part commercialized [38].

The goal of this work is to extend the application of CS to nano-FTIR spectroscopy and -imaging as an enabling tool for spatio-spectral imaging using weak broadband IR sources. Building on the conceptual demonstration of CS for FTIR spectroscopy [39], we adapt CS-FTIR to hyperspectral infrared nano-imaging based on nano-FTIR *s*-SNOM and corresponding complex valued spectra. In addition, the CS approach is augmented by spatial regularization. We demonstrate the performance gain in spatio-spectral imaging of the 6H-SiC phonon band as probe of local mechanical strain in the vicinity of a mechanically induced indent, resolving the associated local spectral shifts of the resonance frequency.

We use broadband synchrotron radiation IR *s*-SNOM (SINS) [14,15] over a spectral range of $\tilde{\nu} = 740\,cm^{-1} - 3200\,cm^{-1}$. We are able to reduce the number of interferometer sampling points to 1/9th *random* samples compared to the original data set, while retaining the spectral content over the full spectral range, specifically the characteristic SiC phonon resonance of interest including its strain induced variation in peak position and linewidth. In contrast, *equidistant* sampling at 1/9th of the original samples leads to a Nyquist limit < 360 cm^{-1}, well below the spectral range covered. This approach paves the way for both rapid spatio-spectral nano-imaging as well as enhanced sensitivity nano-FTIR spectroscopy allowing an order of magnitude longer integration time per image pixel for a gain in spectral content or improvement in detection limit.

2. Methods

2.1 Nano-FTIR spectroscopy

The hyperspectral nano-FTIR measurements were performed on an *s*-SNOM system (Neaspec GmbH, Germany) consisting of an AFM operated in tapping mode and an asymmetric Michelson interferometer, as shown schematically in Fig. 1. The measurements were performed at the electron storage ring Metrology Light Source (MLS) [40], providing ultra-broadband synchrotron IR radiation. The spectral irradiance of the IR radiation emitted by the bending magnet and entering the beamline at a ring current of 200 mA is shown in Fig. 1(a). The radiation is coupled into the *s*-SNOM instrument [14], illuminating Au coated Si cantilevers (Nanosensors™ PPP-NCSTAu, resonance frequency Ω between 120 and 150 kHz), using an off-axis parabolic mirror (f = 11 mm, NA = 0.46, focus diameter ≈80 μm). The tip-scattered IR radiation is recombined with the reference field in a Michelson interferometer with motorized reference arm mirror travelling a distance of 800 μm in this experiment (equivalent to 6.25 cm^{-1} spectral resolution). The interferogram as a function of the optical path difference x is recorded by a liquid nitrogen cooled Mercury-Cadmium-Telluride (MCT) detector (model J15D12M204-S050U-60, Teledyne Judson Technologies, sensitivity 2 – 13.5 μm, i.e., 5000 - 740 cm^{-1}).

Optics EXPRESS

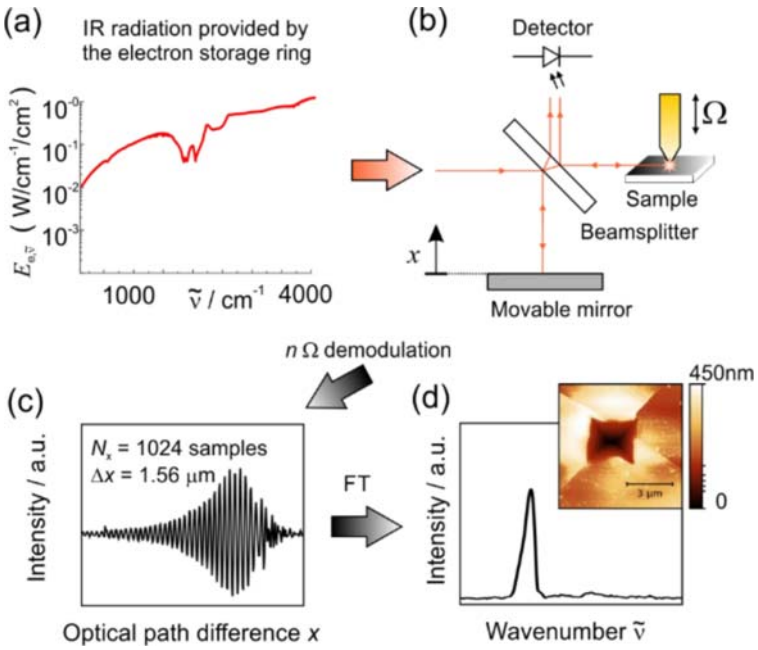

Fig. 1. Experimental setup. The spectral irradiance, $E_{e,\tilde{\nu}}$, of the IR radiation emitted by the electron storage ring MLS is shown in (a). The features around 2000 cm^{-1} originate from the diamond window separating the beamline from the storage ring. The radiation is coupled into an AFM based s-SNOM with a Michelson interferometer (b). The AFM is operated in tapping mode. The detector signal is demodulated at the nth harmonic of the fundamental cantilever frequency Ω to extract the near-field signal, and an interferogram is recorded (c). Fourier transform (FT) yields the spectrum (d), which is spatially mapped using 41 x 44 pixels over an 8 µm by 8 µm scan area of a nanostructured SiC surface. The topography of the indent is shown in the inset.

The detector signal is analyzed by lock-in amplification at the 2nd harmonic 2Ω of the mechanical AFM cantilever resonance frequency Ω as found adequate for s-SNOM near-field extraction from the far-field background [41].

As a sample we choose 6H-SiC(0001) covered by epitaxially grown mono- and bi-layer graphene. The preparation procedure of the graphene growth process involved hydrogen etching which results in parallel terrace structures with heights of ≥ 5 nm and width of several micrometers, as described in [42,43]. The sample surface has been modified by a mechanically induced indent (AFM topography in Fig. 1(d)) causing radially propagating mechanical strain with a corresponding spatially smoothly varying spectral shift and strength of the characteristic optical SiC phonon polariton resonance around 900 cm^{-1} [44]. In addition, the graphene covering the surface leads to additional spatial heterogeneity in the SiC phonon resonance.

Data acquisition was performed to obtain discrete digitized interferograms $I(x)$ with N_x = 1024 equidistant points (Δx = 1.56 µm) which, in standard discrete Fourier transformation (FT) converts to a spectrum $S(\tilde{\nu})$ given by [45]:

$$S\left(k\cdot\Delta\tilde{\nu}\right)=\sum_{n=0}^{N_x-1} I\left(n\cdot\Delta x\right)e^{2\pi i n\frac{k}{N_x}}, \qquad (1)$$

where the optical path difference and the corresponding discrete wavenumber are $x=n\cdot\Delta x$ and $\tilde{\nu}=k\cdot\Delta\tilde{\nu}$, respectively, with spacings $\Delta\tilde{\nu}=1/(N_x\cdot\Delta x)$. The maximum resolvable wavenumber due to aliasing is then given by $\tilde{\nu}_{max}=N_x\cdot\tilde{\nu}/2$, at which the input radiation has

been optically low-pass filtered. With this setup a spectral range from $\tilde{\nu} = 740 cm^{-1}$ (detector limit) to $\tilde{\nu} = 3200 cm^{-1}$ (aliasing limit) can be analyzed, designed to cover spectral signatures from the optical phonon band at low frequencies to upper organic stretch modes (C-H, O-H) at high frequencies. Sequential recording of these spectra by raster scanning of the sample provides a nanoscale resolved hyperspectral image correlated with topography.

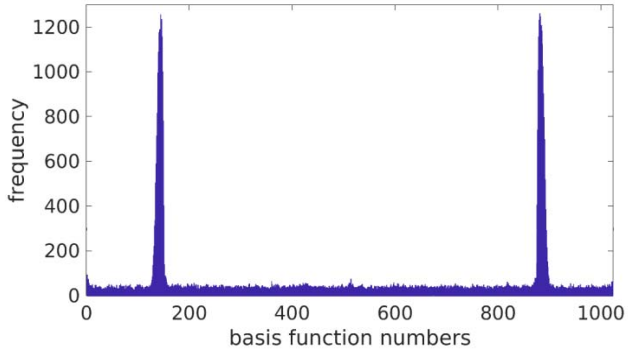

Fig. 2. Histogram of indices of relevant basis functions obtained when subsequently applying compressed sensing to the measurements of each position of the considered array.

2.2 Compressed sensing

Compressed sensing is a new data analysis technique for the efficient recording of a signal that has a sparse representation with respect to some basis [21–26]. The method allows the complete reconstruction of a signal from a reduced number of acquisitions. Rather than sampling the signal at regular intervals as in conventional signal processing, compressed sensing typically selects the acquisitions randomly from the signal. The requirement is that the signal $y(t)$ has a sparse representation in some basis, $\phi_1(t)$, $\phi_2(t),\ldots$, i.e.,

$$y(t) = \sum_{i=1}^{K} z_i \phi_{\pi(i)}(t) \tag{2}$$

where $\phi_{\pi(1)}(t),\ldots,\phi_{\pi(K)}(t)$ denote the K basis functions of the signal $y(t)$ with corresponding weights z. Given a set of measurements, $y(t_1),\ldots,y(t_m)$, the goal is to determine these relevant basis functions. Assume that altogether $n \gg m$ basis functions $\phi_1,\ldots,\phi_n$ are considered, let the m times n matrix A be defined as $A_{ij} = \phi_j(t_i)$, y as the m times 1 vector $(y(t_1),\ldots,y(t_m))^T$, and z as the n times 1 vector of weights, then the following optimization problem is to be solved,

$$\min_z \|z\|_0 \text{ subject to } y = Az, \tag{3}$$

where $\| z \|_0$ denotes the number of nonzero elements of vector z. The solution reveals the relevant basis functions and their weights in the representation (2).

The direct solution of problem (3) is usually not possible for computational reasons. A computationally more feasible optimization problem results from replacing the ℓ_0-norm with the ℓ_1-norm, yielding a convex program [46,47]. Another approach is to use greedy algorithms that provide an approximate solution in short time. One such greedy algorithm is the Orthogonal Matching Pursuit (OMP) algorithm [48] which we have applied.

For hyperspectral imaging, a set of interferograms is recorded for an array of sample positions. Each interferogram is recorded at randomly selected positions of optical path

difference. It can be assumed (see [44]) that each of these spectra is sparse in the Fourier domain (see discussion below). Under this assumption, we apply the OMP algorithm to retrieve a sparse representation in Fourier domain of each recorded spectrum. We then first process the histogram of obtained nonzero coefficients z for all spectra, cf. Figure 2. The figure shows that only a small number of coefficients is relevant for all spectra. We have identified the relevant basis functions as those whose coefficients are nonzero for at least 50% of the spectra. Only these basis functions are then considered. Note that in this way the same basis functions are used at each recording position. Furthermore, the spectra are expected to vary smoothly with respect to the recording position.

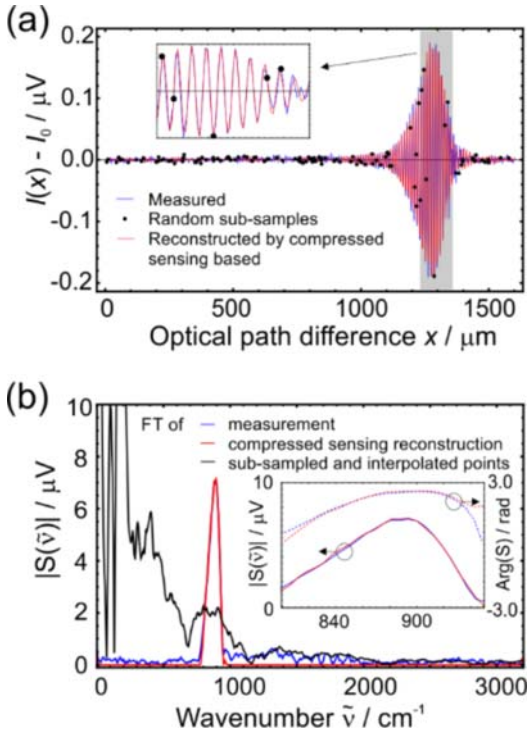

Fig. 3. Example interferogram (a) of measured (blue line), randomly sampled (black dots) and reconstructed (red) data from the randomly sampled points. The inset shows a zoom into a 100 µm long stretch (highlighted in gray) of the optical path difference within the center burst. The corresponding amplitude of the Fourier transform (FT) is shown in (b), comparing the FT based on measured (blue) and reconstructed (red) interferogram data. The black curve shows the FT from the sub-sampled and interpolated data points. The inset plots both amplitude (solid line) and phase (dashed line) of the FT within the spectral region of the phonon peak, showing excellent agreement in both variables between the measured data (blue) and those reconstructed from the subsampled data (red).

The final solution is then obtained by simultaneously fitting the (same) subset of basis functions to all measured spectra, augmented by a regularization functional using the structure matrix of an intrinsic Gauss Markov random field prior [49], which favors similar values for the coefficients of neighboring pixels; 8 neighbors were assigned for interior pixels. The final regularization functional is then taken as the sum of the functionals obtained for each coefficient. The regularization parameter has been determined by the L-curve principle [50].

3. Results and discussion

In order to validate the CS approach using real FTIR nano-spectroscopy and -imaging measurements, the following proceeding was applied. FTIR nano-spectroscopy and -imaging

measurements were conducted using dense, equidistant sampling. The results obtained from these data served as a reference. Subsequently, the complete measured interferogram data were randomly sub-sampled, and these sub-sampled data were taken as input for the CS approach. The results achieved by CS for these sub-sampled data were then compared with the results obtained by a conventional analysis from the complete set of measured data. The evaluation of this approach assumes that the transit time between interferogram positions is small compared to the integration time at each point.

Specifically, a near-field IR interferogram after demodulation and subtraction of a constant offset I_0, with corresponding FT spectrum, are shown in Figs. 3(a) and 3(b) (blue). Usually, the spectra will be referenced to a well characterized reference sample to compensate for instrument response functions or radiation source characteristics. Here, for better clarity, yet without loss of generality, we show the un-referenced spectra. The following three cases are plotted on top of each other: (1) the unmodified measured interferogram (blue line), (2) the N_{sub} = 114 points which have been randomly selected (black dots), and (3) the reconstructed interferogram (red line) by the compressed sensing algorithm using the subsampled data. The reduction to N_{sub} = 114 of randomly selected sampling points corresponds to about 1/9th of the number of originally recorded interferogram points. As seen in the inset of Fig. 3(a) the sampling interval may be as long as several periods of interferogram fringes, implying a substantial loss of spectral information in the conventional interpretation of interferograms. Nevertheless, compressed sensing (red) reconstructs the original spectral content in excellent agreement in amplitude, peak position, and linewidth with the spectrum obtained from FT of the full data set (blue). We expect the level of reduction of 1/9th we obtain to be irrespective of the frequency of the peak position within the considered range of 740 – 3200 cm^{-1}.

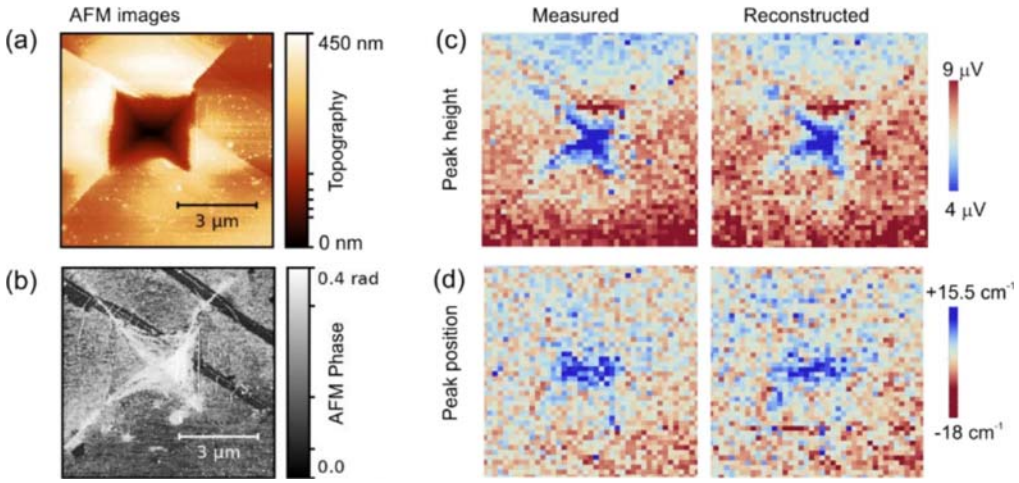

Fig. 4. Spectral mapping of the 6H-SiC surface covered by mono- and bi-layer graphene around a mechanically created indent, shown as a topographical image in (a). Cracks develop as lines from the lower-left to the upper right corner of the image. The lines going from the upper-left to the lower-right corner correspond to terraces on the SiC surface. Close to the terrace edges bi-layer graphene has formed, leading to the dark stripes in the AFM phase image shown in (b). A 41 x 44 array of spectra has been recorded over the area shown in (a). The analysis of peak heights of the SiC-phonon resonance in the spectral region around 900 cm^{-1} results in a 2D map shown in (c) with excellent agreement between measured and reconstructed data. Similarly, the peak position has been analyzed in (d), where the reconstructed data reproduce the main features of the measured data.

A naïve linear interpolation of the sub-sampled interferogram and subsequent FT leads to a complete loss of the spectral information (black line), illustrating the power of the applied compressed sensing algorithm. Note that for in case of N_{sub} = 114 equidistantly sampled

interferogram points the upper wavenumber limit is given by $\tilde{\nu}_{max} = N_x \Delta\tilde{\nu} / 2 < 360 cm^{-1}$, well below the observed spectral feature in Fig. 3(b) between 900 and 1000 cm^{-1}.

The nano-FTIR signal *S* as a coherent process is characterized by both amplitude and phase of the optical response [51]. The inset of Fig. 3(b) shows that within the SiC phonon band also the near-field spectral phase (dashed blue and red lines), is reconstructed accurately.

Deviations of the reconstructed data set from the measured data only lead to a suppression of small spectral features. To evaluate the significance of these deviations for this sample, the 2D spatial maps of peak amplitude and spectral position of the SiC phonon resonance and their strain-induced variations around the mechanical indent are explored, as shown in Fig. 4(a). Note that full sampling in space is performed. The topographical image also shows the typical terraces structures of the SiC surface developed during epitaxial growth of graphene on SiC [42]. The area captured by the image contains mono- and bi-layer graphene areas. The latter are visible in the AFM phase image [43] in Fig. 4(b) as dark stripes located at the terrace edges.

The spatial variations of peak amplitude and spectral position of the SiC phonon resonance comparing the measured (left column) and reconstructed (right column) data are shown in Figs. 4(c) and 4(d). Peak-height features in (c) resulting from residual strain following the indent pattern as well as the bi-layer graphene regions (seen as red stripe running toward the upper left corner) due to surface conduction are well reproduced. The strain-related blue-shifts (d) concentrated in the center of the indent are also well reproduced. This analysis shows that despite the $1/9^{th}$ reduction of sampling points and the slight deviations from the measured data the compressed sensing algorithm reveals the key information of the hyperspectral image.

The presented CS-FTIR approach is based on the assumption of sparsity in the Fourier domain which appears to be well satisfied for the data presented here. In cases where this sparsity is challenged, e.g. through ultra-narrow interferograms, additional fine spectral features, or in cases where the height of the sparse peaks in the Fourier domain are reduced significantly, the approach is expected to yield reduced reconstruction accuracies. Additional knowledge, e.g. about the location of relevant spectral regions, might then be needed in order to stabilize the results. Such an investigation will be subject to future work.

4. Conclusion

We have demonstrated the application of compressed sensing to scattering-type near-field optical microscopy for hyperspectral nano-FTIR imaging. As a scanning probe technique it relies on sequential rastering of a sample surface, which is an inherently inefficient method for recording volume data. We have shown that compressed sensing is a promising route toward more efficient recording of volume data in nano-FTIR spectroscopy. Particular benefit of compressed sensing is expected for *s*-SNOM implementations using ultra-broadband synchrotron radiation. Furthermore, with compressed sensing allowing longer integration times per pixel one may even expect *s*-SNOM spatio-chemical imaging using readily available yet low power thermal globar or other IR continuum sources. It thus promises both rapid and sensitive spatio-chemical nano-imaging for widespread use in academic and industrial settings for fundamental and applied nano- and bio-materials research.

Funding

European Union, Horizon 2020 EMPIR programmes 15HLT01 and 16ENG06 Braunschweig International Graduate School of Metrology (B-IGSM) and NanoMet NSF Science and Technology Center on Real-Time Functional Imaging, DMR-1548924 Alexander von Humboldt Stiftung, Bessel Award

Optics EXPRESS

Acknowledgments

We thank Radek Šlesinger (CMI) for preparing the indentation, as well as Peter Hermann, Piotr Patoka, and Rafael Piestun for fruitful discussions and technical support. The project leading to this application has received funding from the EMPIR programme co-financed by the Participating States and from the European Union's Horizon 2020 research and innovation programme. M.K. acknowledges support from the Braunschweig International Graduate School of Metrology (B-IGSM) and NanoMet. M.B.R acknowledges funding from the NSF Science and Technology Center on Real-Time Functional Imaging under DMR-1548924 and the Bessel Award from the Alexander von Humboldt Foundation.